




Electronic decoupling of polyacenes from the underlying metal substrate by sp^3 carbon atoms

Mohammed S. G. Mohammed ^{1,2,9}, Luciano Colazzo^{1,2,6,7,9}, Roberto Robles ^{2✉}, Ruth Dorel^{3,8}, Antonio M. Echavarren^{3,4}, Nicolás Lorente^{1,2} & Dimas G. de Oteyza ^{1,2,5✉}

On-surface synthesis is becoming an increasingly popular approach to obtain new organic materials. In this context, metallic surfaces are the most commonly used substrates. However, their hybridization with the adsorbates often hinder a proper characterization of the molecule's intrinsic electronic and magnetic properties. Here we report a route to electronically decouple molecules from their supporting substrates. In particular, we have used a Ag (001) substrate and hydrogenated heptacene molecules, in which the longest conjugated segment determining its frontier molecular orbitals amounts to five consecutive rings. The non-planarity that sp^3 atoms impose on the carbon backbone results in electronically decoupled molecules, as demonstrated by scanning tunneling spectroscopy measurements. The charging resonances of the latter imply the presence of double tunneling barriers. We further explain the existing relation between the charging resonance energy and their contrast, as well as with the presence or absence of additional Kondo resonances.

¹Donostia International Physics Center (DIPC), 20018 San Sebastián, Spain. ²Centro de Física de Materiales (CSIC-UPV/EHU)—MPC, 20018 San Sebastián, Spain. ³Institute of Chemical Research of Catalonia (ICIQ), Barcelona Institute of Science and Technology, 43007 Tarragona, Spain. ⁴Departament de Química Orgànica i Analítica, Universitat Rovira i Virgili, 43007 Tarragona, Spain. ⁵Ikerbasque, Basque Foundation for Science, 48013 Bilbao, Spain. ⁶Present address: Center for Quantum Nanoscience, Institute for Basic Science (IBS), Seoul 03760, Republic of Korea. ⁷Present address: Department of Physics, Ewha Womans University, Seoul 03760, Republic of Korea. ⁸Present address: Stratingh Institute for Chemistry, Zernike Institute for Advanced Materials, University of Groningen, Nijenborgh 4, 9747AG Groningen, The Netherlands. ⁹These authors contributed equally: Mohammed S. G. Mohammed, Luciano Colazzo. ✉email: roberto.robles@ehu.es; d_g.oteyza@ehu.es

Polyacenes are a subclass of polyaromatic hydrocarbons that consist of linearly fused benzene rings and attract great attention for fundamental and applied research^{1,2}. They display an important size-dependence in their electronic properties, changing from a closed-shell to a prominent open-shell character as the number of rings increases^{3,4}. The latter confers a high reactivity upon acenes of six or more rings, which makes their synthesis challenging. One of the ways that have been devised to circumvent the synthesis difficulties is the surface-supported synthesis under ultra-high-vacuum (UHV) conditions, which is becoming an increasingly popular approach⁵ and has produced the longest polyacenes to date^{6–16}.

The vacuum environment and the atomically flat metallic surfaces used as substrates further provide excellent conditions for molecular characterization⁵, which can be performed at the single molecule level by scanning probe microscopy. However, when adsorbed on metallic surfaces, hybridization of the molecules with the substrate significantly modifies their properties and leads, at best, to a substantial broadening of the orbitals. Thus, a decoupling of the molecules from the underlying metal substrate becomes not only beneficial but often strictly necessary to characterize the intrinsic molecular properties. A notable example thereof are graphene nanoribbons, which do not show any evidence of their predicted spin-polarized states when adsorbed on metals, but show the associated correlations gaps as soon as they are electronically decoupled from the substrate^{17,18}.

With this decoupling aim, a variety of methods have been applied. Examples include the intercalation of new species between metal and adsorbate (extensively used, e.g., in graphene-based research)^{19–21}, or the use of metal-supported insulating buffer layers as substrates^{17,18,22,23}. The chemical addition of bulky side groups to the molecular structure of interest, which can act as molecule–substrate spacers and thereby reduce their coupling strength, has also been proved successful^{24–26}. The efficiency of this self-decoupling strategy is generally poor due to the flexibility of the carbon backbones, which allows them coming close to the substrate by molecular deformations²⁴. Nevertheless, it has been sufficient, e.g., to regain the functionality of molecular switches that is otherwise quenched by the stronger interaction with the substrate²⁷.

Herein we report the decoupling of polyacenes from an underlying Ag(001) surface by exploiting the non-planarity of the organic backbone imposed by sp^3 -type functional groups. Interestingly, this approach could easily be extrapolated to other organic species and thereby allow important advances in timely research fields like carbon-based magnetism^{28–34}.

Results

Hydrogenated polyacenes as tunable model systems. Hydrogenated polyacene derivatives are stable molecules that can be easily deposited onto clean surfaces by sublimation under UHV conditions and have been used as starting reactants for their transformation into acenes by controlled dehydrogenation^{11,12,14}. As can be discerned in Fig. 1a, b, the hydrogenated rings (imaged by scanning tunneling microscopy (STM) with CO-functionalized probes in the repulsive regime as larger rings (Fig. 1c, d)) feature sp^3 hybridized carbon atoms that break the conjugation along the molecule. It has been demonstrated that the energy gap between the highest occupied molecular orbital (HOMO) and lowest unoccupied molecular orbital (LUMO) of such molecules is ultimately determined by the longest conjugated acene segment, and is remarkably similar to the bandgap of acenes of the same length^{11,12,14}. That is, the dihydrogenated heptacene derivative displayed in Fig. 1b, d, which has been obtained from the controlled tip-induced dehydrogenation of 5,9,14,18-tetrahydroheptacene precursors (Fig. 1a, c)¹¹, features

five rings as the longest conjugated segment and is characterized by a bandgap similar to that of pentacene¹¹. Evidence of the similar electronic properties of 5,18-dihydroheptacene (hereafter referred as dihydroheptacene) and pentacene is provided in Fig. 1e–h, which display calculated low-energy states for the molecules adsorbed on Ag(001). In the case of pentacene, they strongly resemble the LUMO (Fig. 1e) and HOMO (Fig. 1g) of free-standing pentacene²³, and the analogous calculations for dihydroheptacene (Fig. 1f, h) reveal a striking similarity. As such, dihydroheptacene can also be considered a “functionalized pentacene” (2,3-alkylpentacene).

Reference experiments with pentacene. Previous studies of pentacene on Ag(001) have shown the energy-level alignment to be such that the LUMO is aligned with the Fermi energy and consequently partially occupied with an estimated charge of 0.7 electrons³⁵. Any charge transfer-related magnetism is hindered by the substrate: the LUMO is substantially broadened by hybridization with the metal, and the high level of screening reduces electron correlations^{36,37}. In contrast, when the molecule is electronically decoupled from the underlying Ag(001) by a MgO bilayer, the integer charge transfer of one electron to pentacene confers the system a net spin $S = 1/2$ and two spin-split resonances of the former LUMO above and below the Fermi level (the singly occupied (SOMO) and singly unoccupied (SUMO) molecular orbitals, respectively)³⁵.

Evidence for electronic decoupling of dihydroheptacene.

Focusing now on dihydroheptacene on Ag(001), the contrast in STM measurements at low bias values close to the Fermi level (Fig. 1i) resembles the simulated image of the molecular LUMO (Fig. 1j). This underlines again the similarities of dihydroheptacene with pentacene in terms of molecular bandgap and energy-level alignment, with the LUMO energy around E_F . However, it is important to note that there is a great variability in the scanning tunneling spectroscopy (STS) measurements of dihydroheptacene. Figure 2 shows some examples thereof (further examples are displayed in Supplementary Fig. 1). Figure 2a shows a representative dihydroheptacene molecule, marking the typical trajectory along which we record dI/dV point spectra. Stacking their color-coded signals make up datasets like those shown in Fig. 2b–d, which correspond to three different molecules, although all of them sharing the same chemical structure displayed in Fig. 1b. Sample spectra corresponding to the dashed lines (and to the position marked in Fig. 2a) are shown in Fig. 2e. Beyond their markedly different appearance, all datasets present sequences of sharp peaks that shift in position along the molecule. The narrow width of the peaks, their observation beyond the limits of the molecule with a ring-like appearance (i.e., near the molecule but on the bare substrate, Fig. 2f), the electric field dependence of their energy alignment as evidenced by varying tip-sample distance (Supplementary Fig. 2), varying supramolecular environment (Fig. 2f, g), or varying tips (Fig. 2h, i), all together provide unambiguous proof of their nature, namely so-called charging resonances (and associated vibronic satellites³⁸) related to a double tunneling barrier^{38,39}. The presence of a double tunneling barrier implies an effective decoupling of the molecule from the underlying substrate, which is neither expected from molecules in direct contact with transition metal surfaces nor observed for the closely related pentacene on Ag(001).

Here, the key to rationalizing this surprising finding is the presence of the hydrogenated sp^3 C atoms of dihydroheptacene. According to density functional theory (DFT) calculations, in the gas-phase the molecule presents a completely planar C backbone in which the two H atoms bound to each of the sp^3 C atoms

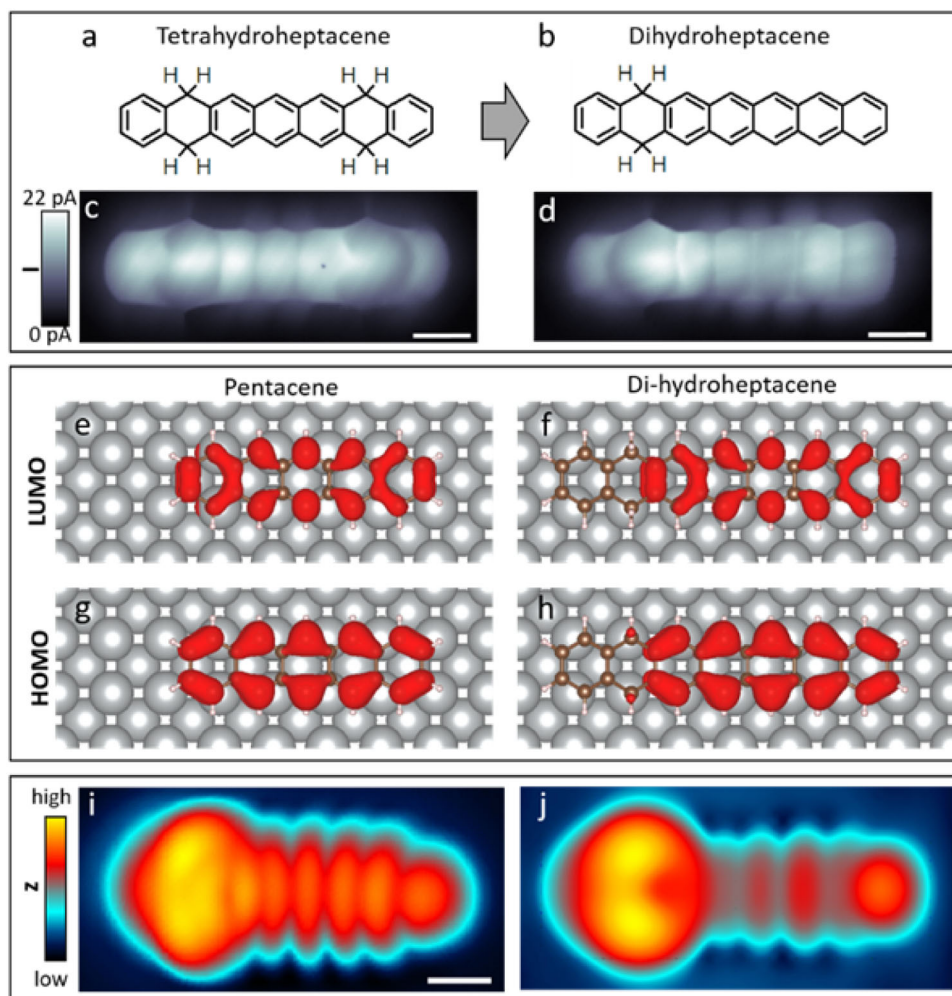


Fig. 1 On-surface synthesis of 5,18-dihydroheptacene and its similarity to pentacene. Chemical structure of 5,9,14,18-tetrahydroheptacene (a) and 5,18-dihydroheptacene (b). Constant height scanning tunneling microscopy (STM) images (sample bias $U = 2$ mV, scale bars = 3 Å) with CO-functionalized probes of 5,9,14,18-tetrahydroheptacene (c) and 5,18-dihydroheptacene (d). Calculated charge densities associated with the highest occupied (HOMO) and lowest unoccupied molecular orbital (LUMO) of pentacene (e, g) and 5,18-dihydroheptacene (f, h). Constant current STM image (imaging parameters: $U = 20$ mV, $I = 100$ pA, scale bar = 4 Å) of 5,18-dihydroheptacene (i) and a simulated STM image of the 5,18-dihydroheptacene LUMO level (j). Note that the differences between experiment (i) and theory (j) arise from the s -wave probe used in the simulations vs. the p -wave character of the CO-functionalized probe used in the measurements²³.

protrude to either side of the plane. Upon adsorption on Ag(001), the symmetry is broken and the hydrogen atoms pointing toward the surface are repelled by steric repulsion. This causes a non-planarity of the molecule as shown in Fig. 2j, which in turn sufficiently reduces its electronic coupling from the substrate to generate the double barrier in the tunneling process.

Origin of charging peaks. In a conventionally pictured double barrier at zero sample bias, there is no electric field across the tunneling junction (Fig. 3a, b). When a positive sample bias U is applied, an electric field is established and a fraction α of the associated potential drops across the barrier between substrate and molecule (Fig. 3c). As a consequence, the molecular orbitals shift up in energy with respect to the substrate's Fermi level by αU . There is a bias threshold U_{th} at which an occupied orbital initially with a binding energy BE can eventually cross the Fermi level ($\alpha U_{th} = BE$) and cause the transfer of an electron to the substrate (Fig. 3d). If the tip-sample distance is reduced (Fig. 3e), the fraction of voltage dropping across the tip-molecule barrier becomes larger, requiring lower bias values

to reach the charge transfer threshold (Fig. 3f). A symmetrically opposite scenario would apply at negative sample bias.

In our measurements, the charging resonances shift in the same direction (to lower sample bias values) when reducing the tip-sample distance (Supplementary Fig. 2) and display the same concave curvature in the stacked spectra regardless of whether they appear at positive (Fig. 2d) or negative (Fig. 2b) bias. In fact, the curved charging resonance trajectory along the molecule often crosses the Fermi level (Fig. 2c). This is inconsistent with the common assumption of a zero electric field at zero bias and instead implies that, at least in cases like Fig. 2b, c, the zero electric field condition occurs at negative sample bias, in particular more negative than the “charging peak parabola” onset. This is understood in a straightforward manner assuming different work functions for tip and sample (Fig. 3g), which establish a contact potential difference and the associated electric field when brought into tunneling distance (Fig. 3h). Under these circumstances, the charging threshold may indeed be observed at negative bias values (Fig. 3i) and the zero electric field bias (Fig. 3j) corresponds to that typically measured in Kelvin probe force microscopy, which in most of the cases differs from zero and varies with both tip and sample⁴⁰.

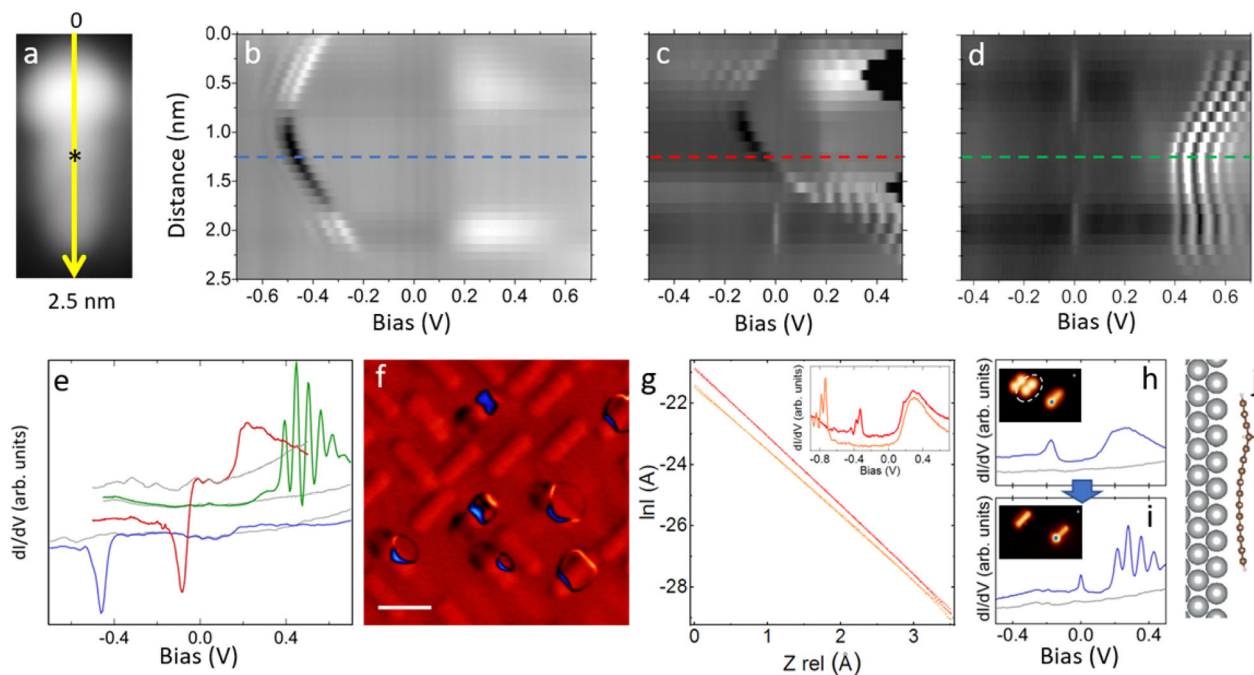


Fig. 2 Varying spectroscopic fingerprints. **a** Constant current scanning tunneling microscopy (STM) image of 5,18-dihydroheptacene. Stacked differential conductance (dI/dV) point spectra with color-coded signal (at each point the feedback loop is adjusted to sample bias (U) and current (I) tunneling parameters $U = 200$ mV, $I = 200$ pA (**b**), $U = 50$ mV, $I = 250$ pA (**c**), and $U = 50$ mV, $I = 100$ pA (**d**)). Each panel corresponds to measurements on different molecules sharing the same structure along a trajectory similar to that outlined by the yellow line in **a**. **e** Selected dI/dV point spectra extracted from **b-d** at the position of the dashed lines (colored accordingly in **b-d**) and the asterisk in **a**. **f** Constant current dI/dV map (imaging parameters $U = -80$ mV, $I = 200$ pA, scale bar = 2 nm) of a sample containing multiple molecular species including several 5,18-dihydroheptacene molecules. **g** Current (I) vs. the relative tip height distance (z) spectra on two different 5,18-dihydroheptacene molecules. The reference for z is the tip-sample distance at which the feedback was opened on either molecule, with tunneling parameters $U = 20$ mV, $I = 780$ pA for the red curve and $U = 20$ mV, $I = 388$ pA for the orange curve. The inset displays the associated dI/dV spectra on those same molecules. **h** dI/dV point spectrum on a 5,18-dihydroheptacene molecule (blue line) and a reference spectrum on the substrate (gray line) at the positions marked by accordingly colored points in the inset. **i** Similar dI/dV point spectra taken at the same positions after functionalizing the tip with the 5,9,14,18-tetrahydroheptacene molecule marked with the white oval in the inset of **h**. **j** Structure of 5,18-dihydroheptacene relaxed on Ag(001) as simulated by density functional theory. All dI/dV spectra and maps are acquired with a Lock-in frequency $\omega = 731$ Hz and amplitude $U_{osc} = 10$ mV, except $U_{osc} = 5$ mV for **d**.

Relation of the charging peaks with the Kondo resonance. We can thus now conclude that for this system, the charging resonance involves in all cases (whether at positive or negative bias values) the same molecular orbital, namely the LUMO. It is close in energy to E_F and can thus be easily brought across the substrate's Fermi level by electric fields at the tunneling junction. At the time of the tunneling event across the tip-molecule barrier, the LUMO is empty or occupied at bias values above or below that of the charging resonance, respectively. For that reason, whenever the zero bias point coincides with a molecule in its charged state (occupied LUMO), an additional zero bias resonance appears in the spectra (Fig. 2c, d), but not if the molecule at zero bias is in its neutral state (Fig. 2b, c). As opposed to the charging resonances, this zero bias resonance does not shift for varying tip heights (Supplementary Fig. 2b) and is a manifestation of the Kondo effect associated with the spin 1/2 of the molecule as a single electron occupies its gas-phase LUMO^{41,42}. This is confirmed by its anomalously fast broadening with temperature, whose width evolution is in agreement with a Kondo temperature of 73 ± 2 K (Supplementary Fig. 3 and Supplementary Note 1). The presence of this Kondo resonance is further proof of the decoupling effect that the “pentacene functionalization” at C-2 and C-3 with sp^3 carbon atoms brings about. If that were not the case, a broader LUMO level and reduced electron correlations would cause an equal population of spin up and spin down LUMO orbitals^{36,37}, resulting in no net spin and no Kondo peak,

as occurs with pristine pentacene³⁵. On the other hand, the Kondo resonance still implies a minor molecule–substrate coupling, since it relates to the screening of the molecular spin by the substrate electrons and would thus be absent for a more efficient decoupling as observed for pentacene on an insulating MgO buffer layer. We can thus conclude that on Ag(001), the “pentacene functionalization” by sp^3 carbon atoms results in sufficiently decoupled molecules to show charging resonances and stabilize a singly charged molecule with net spin 1/2, but with sufficient molecule–substrate interaction to reveal a Kondo resonance. In other words, more decoupled than pristine pentacene on Ag(001) but, as could be expected, less than pentacene on a MgO bilayer on Ag(001).

Variability of the charging resonance energies. A question that arises at this point, however, is where the large variability displayed by the charging resonances comes from. Being an electric field-driven effect, it largely depends on the tip, on the sample, as well as on the contact potential difference between them. Different tips (in terms of shape, but also tip apex functionalization)⁴⁰ will notably impact the electric field lines within the tunneling junction and thus the charging resonance appearance. By way of example, Fig. 2h shows the conductance spectrum obtained with a metallic tip on the “functionalized pentacene” molecule marked with a blue point in the inset. The charging peak appears at negative bias. Consequently, at zero bias the molecule is in its neutral state and

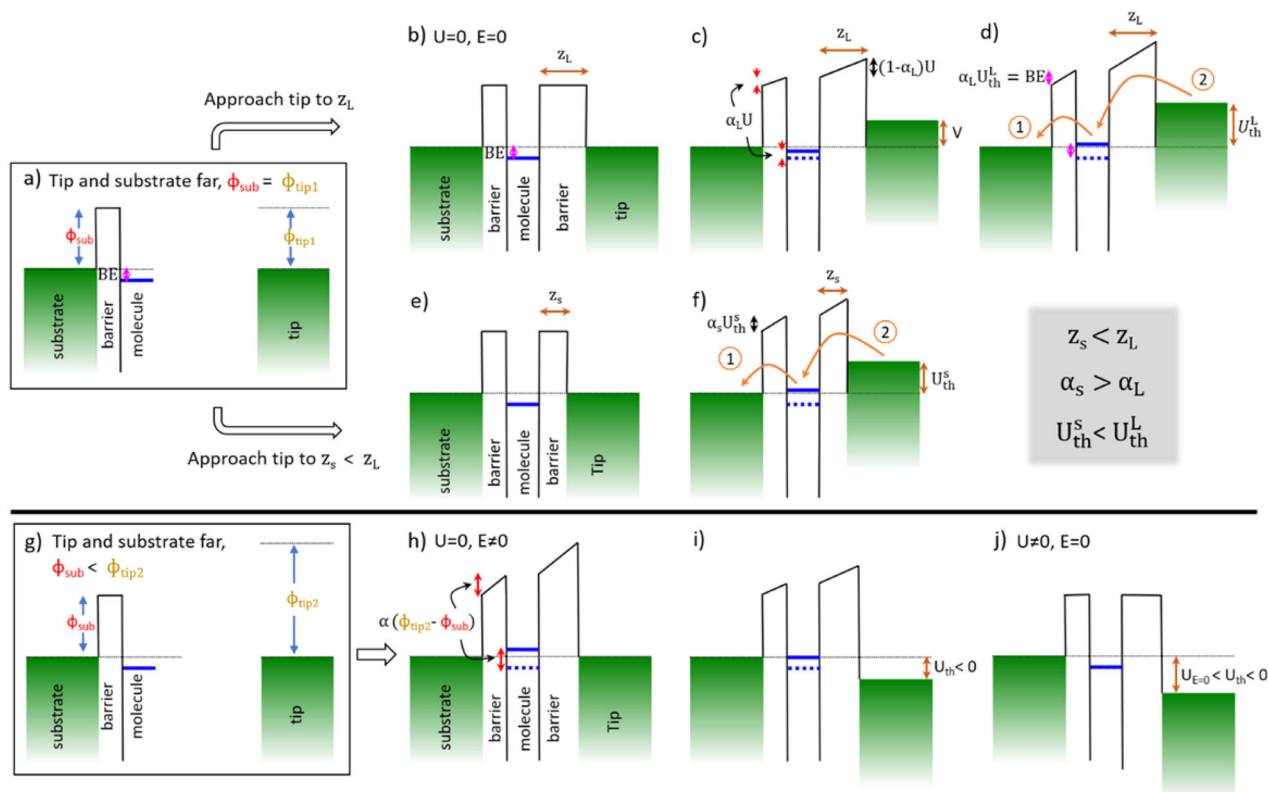


Fig. 3 Schematic energy diagram of a double tunneling barrier. **a** The barrier’s elements are a molecule with an occupied molecular orbital at a binding energy (BE) marked by a blue line, adsorbed on a substrate of workfunction ϕ_{sub} , and a tip of workfunction $\phi_{\text{tip1}} = \phi_{\text{sub}}$, which are initially far from one another. **b** Energy diagram after bringing the tip into a tunneling distance z_L of the molecule at zero bias U and zero electric field E and **(c)** after application of a sample bias U , displaying a potential drop of αU across the molecule–substrate barrier. **d** Diagram at the charging bias threshold U_{th}^L , at which a tunneling current sets in that is associated with an initial electron transfer from the occupied molecular orbital to the substrate (1), followed by an electron transfer from the tip to the transiently unoccupied orbital (2). **e** Comparative energy diagram with a smaller tip–molecule distance $z_s < z_L$ without and **(f)** with an applied bias that coincides with the charging threshold $U_{\text{th}}^s < U_{\text{th}}^L$ at which a similar electron tunneling scenario sets in as described for **d**. The associated proportionality of the potential drop across the molecule–substrate barrier α is larger for smaller tip–sample distances ($\alpha_s > \alpha_L$). **g** Double tunneling barrier elements featuring a tip with larger workfunction $\phi_{\text{tip2}} > \phi_{\text{sub}}$. **h** Electric field E and shift of the formerly occupied molecular orbital energy by $\alpha(\phi_{\text{tip2}} - \phi_{\text{sub}})$ to an energy above the Fermi level as the tip is approached to the sample even in the absence of an applied bias U . **i** Diagram at the negative sample bias threshold for the orbital’s charging. **j** Diagram at the negative bias required to nullify the electric field E across the double tunneling barrier.

no Kondo peak is observed. As the tip is functionalized by picking up the molecule marked with the white oval, the tip’s workfunction and the overall electric field at the tunneling junction change. As a result, a conductance spectrum taken on the same molecule as in panel (h) now shows the charging resonances at positive bias (Fig. 2i). The molecule is therefore charged at zero bias at the time of the tunneling between tip and molecule, and consequently displays a Kondo peak.

However, not only the tip matters for the charging resonance appearance, but also inhomogeneities in the sample. The tunneling barrier and the electric field within the tunneling junction are also affected by the polarizability of a molecule’s surroundings (neighboring molecules, surface, subsurface defects, etc.)^{42–46}. Therefore, even with the same tip, molecules sharing the same structure may display different charging peaks⁴². A conductance map measured at -80 mV on a variety of hydrogenated heptacene derivatives¹¹ displays, on each of the “functionalized pentacene” molecules, charging rings with different shapes and sizes that are even centered on different molecular positions (Fig. 2f). Similar changes are found for a same molecule after tip manipulation to another epitaxially equivalent substrate position. STS data acquired with the same tip on equivalent positions of different “functionalized pentacene”

molecules are shown in Fig. 2g. The inset displays the dI/dV spectra, revealing charging resonances at very different bias values. Associated I vs. z curves taken at the same positions reveal the expected linear behavior when the current is plotted logarithmically, and notably different slopes (Fig. 2i). The slopes correlate with the effective barrier at the tunneling junction, which is typically associated with an average of tip and sample workfunction⁴⁷. The tip being the same, we can conclude that the change in the effective barrier relates to local inhomogeneities in the substrate⁴² and/or local supramolecular environment^{43–46}, resulting in this particular case in a 0.51 eV larger effective tunneling barrier and 0.4 V lower charging bias threshold for the molecule associated with the red curves.

Understanding the varying contrast of charging resonances.

When the charging resonances occur at positive bias, they appear everywhere as a sharp maximum (Fig. 2d). Interestingly, the charging resonances at negative bias instead show a location-dependent appearance, namely as a peak near the molecular ends and as a dip around the “pentacene” segment’s center or on the substrate (Fig. 2b, c). The same effect can be observed in conductance maps of the charging rings. When they appear at

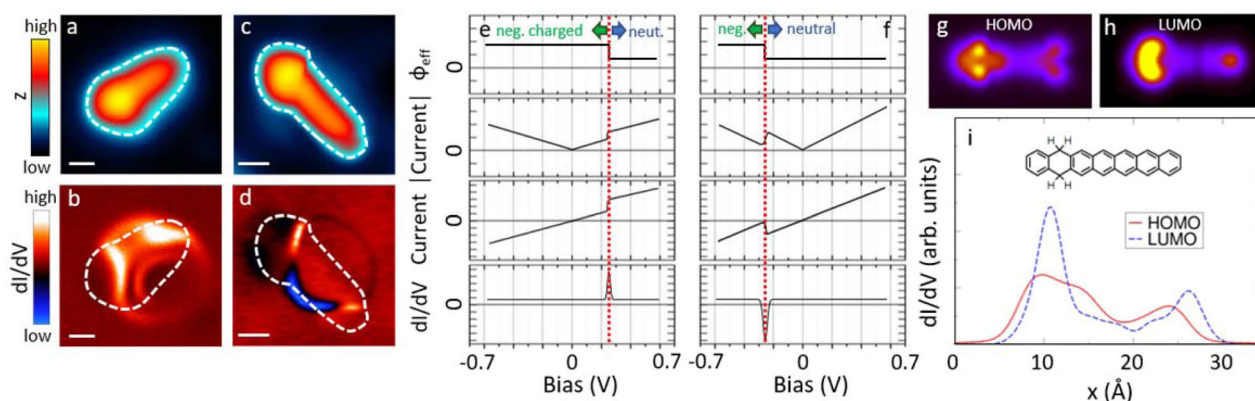


Fig. 4 Observation and understanding of the charging resonance contrast variability. Constant current scanning tunneling microscopy (STM) (a) and simultaneously acquired differential conductance (dI/dV) signal (b) of a 5,18-dihydroheptacene molecule displaying the charging resonances at positive bias (tunneling parameters in a, b; sample bias $U = 615$ mV, current $I = 80$ pA, lock-in bias oscillation $U_{osc} = 10$ mV); and equivalent STM (c) and dI/dV (d) measurements for a molecule displaying the charging resonances negative bias (c, d; $U = -80$ mV, $I = 200$ pA, lock-in bias oscillation $U_{osc} = 10$ mV). The periphery of the molecule as imaged by constant current STM is marked with a white dashed line and superimposed on the dI/dV images for comparison. The associated scale bars correspond to 5 Å in all four images and the color scales are displayed on the left. Schematic graphs of the expected current modulus, current, and dI/dV signal evolution associated with the effective tunneling barrier modification ϕ_{eff} as a molecule reaches its charging threshold (marked by a red dotted line) at positive (e) and negative bias (f). Simulated dI/dV maps at 10 Å above the molecular plane at the highest occupied (HOMO) (g) and lowest unoccupied molecular orbital (LUMO) (h) energies. i Comparative cross section of the calculated dI/dV signal along the long molecular axis at 10 Å above the molecular plane (the molecular structure inset is drawn to scale for guidance).

positive bias, the charging rings (and their concentric vibronic satellites) are imaged everywhere as a conductance increase (Fig. 4a, b). Instead, charging rings at negative bias are imaged with a reduced conductance signal on the substrate, an even stronger reduction around the “pentacene” segment’s center, and with an increased conductance signal near its ends (Fig. 4c, d). We rationalize these findings as follows.

As an adsorbate becomes charged with an electron (hole) from the surface, that charge redistribution causes an interfacial dipole that increases (decreases) the effective tunneling barrier. In our experiments, at bias values below that of the charging resonance, the tunneling process between tip and molecule involves a molecular species charged with an extra electron. Such charge transfer causes an interface dipole that increases the tunneling barrier and thus reduces the associated tunneling current. As the molecule becomes neutral at higher bias values, the barrier decreases and the tunneling current increases. While at positive bias values, this increase in current results in a sharp peak in the dI/dV signal (Fig. 4e), a similar increase of the tunneling intensity at negative bias appears as a dip (Fig. 4f). Taking these considerations into account we would expect the charging resonances to appear everywhere as dips at negative bias and as peaks at positive bias.

However, there is an additional effect to consider. In a singly charged molecule, the lowest energy states are the SOMO and the SUMO, both of them related to the gas-phase LUMO. Instead, for a neutral molecule the frontier orbitals are the HOMO and the LUMO. That is, the unoccupied frontier states for charged and neutral molecules share the same wavefunction symmetry and spatial distribution of the gas-phase LUMO. Thus, for positive bias values on either side of the charging resonance, the orbitals involved in the tunneling (whether resonantly or only through the electronic state’s tails) are always dominantly LUMO related.

Focusing on the occupied states, the frontier orbital for charged and neutral molecules relate to the gas-phase LUMO and HOMO, respectively. Thus, for negative bias values, on either side of the charging resonance, two different orbitals with disparate wavefunction symmetry and spatial distribution are involved in the tunneling process. Their decay perpendicular to

the surface plane (Fig. 4g, h) and consequently the tunneling transmission function between tip and molecule is locally very different. At the same tip height, it is the HOMO that provides a larger transmission in the central region of the “functionalized pentacene”, while it is the LUMO on the outer sides of the molecule (Fig. 4i). This has a strong impact on the measured conductance as the charging resonance is crossed, while ramping up the bias and the orbital dominating the tunneling process changes from the gas-phase LUMO to the gas-phase HOMO: the conductance signal near the molecular ends increases, whereas it decreases near the center of the “pentacene” segment.

This effect is convoluted with that described earlier of the different tunneling barrier at either side of the charging resonance. At negative bias, the latter imprints a dip-like appearance to the charging resonances on the substrate nearby the molecules (Fig. 4d). As the tip moves onto the molecules and the molecular orbitals become directly involved in the tunneling process, the modified tunneling transmission promotes the dip on the central region of the molecule (Fig. 4d). In contrast, on the outer regions of the molecule it reduces the current as the charging threshold is crossed, compensating and even reverting the effect of the lower effective tunneling barrier on neutral molecules, thus finally appearing as a dI/dV peak in those regions.

Discussion

Besides providing an understanding of why charging resonances appear as peaks or dips depending on the polarity and spatial location on the molecules, we have characterized the critical effect of sp^3 carbon atoms along the backbone of acene derivatives on their electronic decoupling from the supporting substrates. The non-planarity imposed by the sp^3 carbon atoms drives an electronic decoupling from the underlying substrate that has been shown to be sufficient to establish a double tunneling barrier and stabilize a singly charged molecule holding a net spin $S = 1/2$. Importantly, although the experiments have been performed on hydrogenated heptacene molecules, this concept may be transposed to many other polyaromatic hydrocarbons of great scientific interest.

Methods

Experimental. The precursor synthesis has followed the process described in reference¹¹. The sample has been prepared by firstly cleaning the Ag(001) surface using Ar⁺ sputtering at 5E – 6 mBar and 0.8 KeV followed by annealing to 670 K applying multiple cycles until the surface is cleaned. Secondly, a handmade Knudsen cell evaporator has been used for subliming the precursor 5,9,14,18-tetrahydroheptacene molecules at 453 K. Finally, for CO functionalization of the STM tip, NaCl has been deposited on the sample by sublimation at 783 K, then the sample has been cooled to 4.3 K for CO deposition. For the latter, the sample is clamped in its cooling position, a CO partial pressure of 8E – 9 mBar is introduced in the STM chamber via a leak valve, and the cryostat shields are opened for about 80 s in various “open-close” cycles to avoid the maximum temperature to raise above 7.2 K. STM measurements have been performed on a commercial LT-STM (Scienta-Omicron) under UHV conditions and operating at 4.3 K. The partial dehydrogenation of the starting reactant is achieved as described in reference¹¹ either by controlled annealing treatments or by tip-induced dehydrogenation. Unless stated specifically in the paper, Pt/Ir tip has been used for acquiring the experimental STM and STS data, which has been optimized by poking into the metal surface for sharpening. A digital lock-in modulator with a modulation frequency of 731 Hz has been employed for dI/dV measurements. STM images have been analyzed using WSxM software⁴⁸.

Theoretical. Ab initio calculations have been performed in the framework of DFT as implemented in the VASP code^{49,50}. Core electrons have been treated within the projector augmented-wave method⁵¹. Wavefunctions have been expanded using a plane wave basis set with an energy cutoff of 400 eV. For the exchange and correlation functional, we have used the generalized gradients approximation in the PBE flavor⁵². Missing van der Waals interactions in this functional have been included following the Tkatchenko–Scheffler scheme⁵³. The Ag(001) surface has been simulated using a 12 × 7 unit cell with 5 Ag layers and a vacuum layer of 15 Å. The atoms in three upper layers of the slab and in the molecules have been relaxed until all the forces were below 0.01 eV/Å. STM topographic images and simulated dI/dV maps have been calculated using the Tersoff and Hamann approximation⁵⁴ as described by Bocquet et al.⁵⁵ and implemented in the STMpw code⁵⁶. Although using the Γ -point to sample the Brillouin zone is enough for most calculations due to the size of the unit cell, an increased 2 × 3 × 1 k-mesh has been used for the STM simulations. Images of charge densities and DFT models have been generated using the VESTA code⁵⁷.

Data availability

The data that support the findings of this study are available from the corresponding authors upon reasonable request.

Code availability

The codes used for the theoretical calculations in this study are available from the associated references.

Received: 21 April 2020; Accepted: 14 August 2020;

Published online: 15 September 2020

References

- Anthony, J. E. Functionalized acenes and heteroacenes for organic electronics. *Chem. Rev.* **106**, 5028–5048 (2006).
- Anthony, J. E. The larger acenes: versatile organic semiconductors. *Angew. Chem. Int. Ed.* **47**, 452–483 (2008).
- Bendikov, M. et al. Oligoacenes: theoretical prediction of open-shell singlet diradical ground states. *J. Am. Chem. Soc.* **126**, 7416–7417 (2004).
- Hachmann, J., Dorando, J. J., Avilés, M. & Chan, G. K.-L. The radical character of the acenes: a density matrix renormalization group study. *J. Chem. Phys.* **127**, 134309 (2007).
- Clair, S. & de Oteyza, D. G. Controlling a chemical coupling reaction on a surface: tools and strategies for on-surface synthesis. *Chem. Rev.* **119**, 4717–4776 (2019).
- Krüger, J. et al. Tetracene formation by on-surface reduction. *ACS Nano* **10**, 4538–4542 (2016).
- Dinca, L. E. et al. Unprecedented transformation of tetrathienanthracene into pentacene on Ni(111). *ACS Nano* **7**, 1652–1657 (2013).
- Krüger, J. et al. Imaging the electronic structure of on-surface generated hexacene. *Chem. Commun.* **53**, 1583–1586 (2017).
- Urgel, J. I. et al. On-surface synthesis of heptacene organometallic complexes. *J. Am. Chem. Soc.* **139**, 11658–11661 (2017).
- Zugermeier, M. et al. On-surface synthesis of heptacene and its interaction with a metal surface. *Nanoscale* **9**, 12461–12469 (2017).
- Colazzo, L. et al. On-surface synthesis of heptacene on Ag(001) from brominated and non-brominated tetrahydroheptacene precursors. *Chem. Commun.* **54**, 10260–10263 (2018).
- Zuzak, R. et al. Nonacene generated by on-surface dehydrogenation. *ACS Nano* **11**, 9321–9329 (2017).
- Krüger, J. et al. Decacene: on-surface generation. *Angew. Chem. Int. Ed.* **56**, 11945–11948 (2017).
- Zuzak, R. et al. Higher acenes by on-surface dehydrogenation: from heptacene to undecacene. *Angew. Chem. Int. Ed.* **57**, 10500–10505 (2018).
- Urgel, J. I. et al. On-surface light-induced generation of higher acenes and elucidation of their open-shell character. *Nat. Commun.* **10**, 861 (2019).
- Eisenhut, F. et al. Dodecacene generated on surface: reopening of the energy gap. *ACS Nano* **14**, 1011–1017 (2020).
- Ruffieux, P. et al. On-surface synthesis of graphene nanoribbons with zigzag edge topology. *Nature* **531**, 489–492 (2016).
- Wang, S. et al. Giant edge state splitting at atomically precise graphene zigzag edges. *Nat. Commun.* **7**, 11507 (2016).
- Riedl, C., Coletti, C., Iwasaki, T., Zakharov, A. A. & Starke, U. Quasi-free-standing epitaxial graphene on SiC obtained by hydrogen intercalation. *Phys. Rev. Lett.* **103**, 246804 (2009).
- Palacio, I. et al. Reversible graphene decoupling by NaCl photo-dissociation. *2D Mater.* **6**, 025021 (2019).
- Deniz, O. et al. Revealing the electronic structure of silicon intercalated armchair graphene nanoribbons by scanning tunneling spectroscopy. *Nano Lett.* **17**, 2197–2203 (2017).
- Repp, J., Meyer, G., Stojković, S. M., Gourdon, A. & Joachim, C. Molecules on insulating films: scanning-tunneling microscopy imaging of individual molecular orbitals. *Phys. Rev. Lett.* **94**, 026803 (2005).
- Gross, L. et al. High-resolution molecular orbital imaging using a p-wave STM tip. *Phys. Rev. Lett.* **107**, 086101 (2011).
- Moresco, F. & Gourdon, A. Scanning tunneling microscopy experiments on single molecular landers. *Proc. Natl Acad. Sci.* **102**, 8809–8814 (2005).
- Matino, F. et al. Electronic decoupling of a cyclophane from a metal surface. *Proc. Natl Acad. Sci.* **108**, 961–964 (2011).
- Aleman, M. et al. Electric field-induced isomerization of azobenzene by STM. *J. Am. Chem. Soc.* **128**, 14446–14447 (2006).
- Comstock, M. J. et al. Reversible photomechanical switching of individual engineered molecules at a metallic surface. *Phys. Rev. Lett.* **99**, 038301 (2007).
- Mishra, S. et al. Topological frustration induces unconventional magnetism in a nanographene. *Nat. Nanotechnol.* **15**, 22–28 (2020).
- Li, J. et al. Single spin localization and manipulation in graphene open-shell nanostructures. *Nat. Commun.* **10**, 200 (2019).
- Mishra, S. et al. Topological defect-induced magnetism in a nanographene. *J. Am. Chem. Soc.* **142**, 1147–1152 (2020).
- Pavliček, N. et al. Synthesis and characterization of triangulene. *Nat. Nanotechnol.* **12**, 308–311 (2017).
- Mishra, S. et al. Synthesis and characterization of π -extended triangulene. *J. Am. Chem. Soc.* **141**, 10621–10625 (2019).
- Lawrence, J. et al. Probing the magnetism of topological end states in 5-armchair graphene nanoribbons. *ACS Nano* **14**, 4499–4508 (2020).
- Li, J. et al. Uncovering the triplet ground state of triangular graphene nanoflakes engineered with atomic precision on a metal surface. *Phys. Rev. Lett.* **124**, 177201 (2020).
- Hollerer, M. et al. Charge transfer and orbital level alignment at inorganic/organic interfaces: the role of dielectric interlayers. *ACS Nano* **11**, 6252–6260 (2017).
- Anderson, P. W. Localized magnetic states in metals. *Phys. Rev.* **124**, 41–53 (1961).
- Ternes, M., Heinrich, A. J. & Schneider, W.-D. Spectroscopic manifestations of the Kondo effect on single adatoms. *J. Phys. Condens. Matter* **21**, 053001 (2009).
- Nazin, G. V., Wu, S. W. & Ho, W. Tunneling rates in electron transport through double-barrier molecular junctions in a scanning tunneling microscope. *Proc. Natl Acad. Sci.* **102**, 8832–8837 (2005).
- Mikaelian, G., Ogawa, N., Tu, X. W. & Ho, W. Atomic scale control of single molecule charging. *J. Chem. Phys.* **124**, 131101 (2006).
- Gross, L. et al. Investigating atomic contrast in atomic force microscopy and Kelvin probe force microscopy on ionic systems using functionalized tips. *Phys. Rev. B* **90**, 155455 (2014).
- Kumar, A. et al. Charge-transfer-driven nonplanar adsorption of F 4 TCNQ molecules on epitaxial graphene. *ACS Nano* **11**, 4960–4968 (2017).
- Fernández-Torrente, I., Kreikemeyer-Lorenzo, D., Stróžeczka, A., Franke, K. J. & Pascual, J. I. Gating the charge state of single molecules by local electric fields. *Phys. Rev. Lett.* **108**, 036801 (2012).
- Cochrane, K. A., Schiffrin, A., Roussy, T. S., Capsoni, M. & Burke, S. A. Pronounced polarization-induced energy level shifts at boundaries of organic semiconductor nanostructures. *Nat. Commun.* **6**, 8312 (2015).

44. Goiri, E. et al. Self-assembly of bicomponent molecular monolayers: adsorption height changes and their consequences. *Phys. Rev. Lett.* **112**, 117602 (2014).
45. Borghetti, P. et al. Spectroscopic fingerprints of work-function-controlled phthalocyanine charging on metal surfaces. *ACS Nano* **8**, 12786–12795 (2014).
46. Goiri, E., Borghetti, P., El-Sayed, A., Ortega, J. E. & de Oteyza, D. G. Multi-component organic layers on metal substrates. *Adv. Mater.* **28**, 1340–1368 (2016).
47. Vitali, L. et al. Portrait of the potential barrier at metal–organic nanocontacts. *Nat. Mater.* **9**, 320–323 (2010).
48. Horcas, I. et al. WSXM: a software for scanning probe microscopy and a tool for nanotechnology. *Rev. Sci. Instrum.* **78**, 013705 (2007).
49. Kresse, G. & Furthmüller, J. Efficiency of ab-initio total energy calculations for metals and semiconductors using a plane-wave basis set. *Comput. Mater. Sci.* **6**, 15–50 (1996).
50. Kresse, G. & Joubert, D. From ultrasoft pseudopotentials to the projector augmented-wave method. *Phys. Rev. B* **59**, 1758–1775 (1999).
51. Blöchl, P. E. Projector augmented-wave method. *Phys. Rev. B* **50**, 17953–17979 (1994).
52. Perdew, J. P., Burke, K. & Ernzerhof, M. Generalized gradient approximation made simple. *Phys. Rev. Lett.* **77**, 3865–3868 (1996).
53. Tkatchenko, A. & Scheffler, M. Accurate molecular Van Der Waals interactions from ground-state electron density and free-atom reference data. *Phys. Rev. Lett.* **102**, 073005 (2009).
54. Tersoff, J. & Hamann, D. R. Theory of the scanning tunneling microscope. *Phys. Rev. B* **31**, 805–813 (1985).
55. Bocquet, M.-L., Lesnard, H., Monturet, S. & Lorente, N. Theory of elastic and inelastic electron tunneling. In *Computational Methods in Catalysis and Materials Science* (eds van Santen, R. A. & Sautet, P.) 199–219 (Wiley-VCH Verlag GmbH & Co. KGaA, 2009). <https://doi.org/10.1002/9783527625482.ch11>.
56. Lorente, N. & Robles, R. STMpw (Zenodo, 2019). <https://doi.org/10.5281/ZENODO.3581159>.
57. Momma, K. & Izumi, F. VESTA 3 for three-dimensional visualization of crystal, volumetric and morphology data. *J. Appl. Crystallogr.* **44**, 1272–1276 (2011).

Acknowledgements

This project has received funding from the European Union's Horizon 2020 research and innovation program under Grant Agreement Nos. 635919 (ERC-StG), 837225 (ERC-

PoC), and 766864 (FET-Open), from the Spanish Agencia Estatal de Investigación (Grant Nos. MAT2016-78293-C6, PID2019-104815GB-I00 and PID2019-107338RB-C63), from AGAUR (2017 SGR 1257), and from the CERCA, Program/Generalitat de Catalunya. We thank Alex Riss for interesting discussions.

Author contributions

M.S.G.M, L.C, and D.G.O performed the STM and STS measurement and analysis. R.D and A.M.E. synthesized the molecules. R.R. and N.L. performed the calculations. All authors contributed to the discussion and preparation of the manuscript.

Competing interests

The authors declare no competing interests.

Additional information

Supplementary information is available for this paper at <https://doi.org/10.1038/s42005-020-00425-y>.

Correspondence and requests for materials should be addressed to R.R. or D.G.d.O.

Reprints and permission information is available at <http://www.nature.com/reprints>

Publisher's note Springer Nature remains neutral with regard to jurisdictional claims in published maps and institutional affiliations.



Open Access This article is licensed under a Creative Commons Attribution 4.0 International License, which permits use, sharing, adaptation, distribution and reproduction in any medium or format, as long as you give appropriate credit to the original author(s) and the source, provide a link to the Creative Commons license, and indicate if changes were made. The images or other third party material in this article are included in the article's Creative Commons license, unless indicated otherwise in a credit line to the material. If material is not included in the article's Creative Commons license and your intended use is not permitted by statutory regulation or exceeds the permitted use, you will need to obtain permission directly from the copyright holder. To view a copy of this license, visit <http://creativecommons.org/licenses/by/4.0/>.

© The Author(s) 2020